Check for updates

# Fast Wide-Field Quantum Sensor Based on Solid-State Spins Integrated with a SPAD Array

*Guoqing Wang,\* Francesca Madonini, Boning Li, Changhao Li, Jinggang Xiang, Federica Villa, and Paola Cappellaro\**

Achieving fast, sensitive, and parallel measurement of a large number of quantum particles is an essential task in building large-scale quantum platforms for different quantum information processing applications such as sensing, computation, simulation, and communication. Current quantum platforms in experimental atomic and optical physics based on CMOS sensors and charged coupled device cameras are limited by either low sensitivity or slow operational speed. Here an array of single-photon avalanche diodes is integrated with solid-state spin defects in diamond to build a fast wide-field quantum sensor, achieving a frame rate up to 100 kHz. The design of the experimental setup to perform spatially resolved imaging of quantum systems is presented. A few exemplary applications, including sensing DC and AC magnetic fields, temperature, strain, local spin density, and charge dynamics, are experimentally demonstrated using a nitrogen-vacancy ensemble diamond sample. The developed photon detection array is broadly applicable to other platforms such as atom arrays trapped in optical tweezers, optical lattices, donors in silicon, and rare earth ions in solids.

G. Wang, F. Madonini, B. Li, C. Li, J. Xiang, P. Cappellaro
Research Laboratory of Electronics
Massachusetts Institute of Technology
Cambridge, MA 02139, USA
E-mail: gq_wang@mit.edu; pcappell@mit.edu
G. Wang, C. Li, P. Cappellaro
Department of Nuclear Science and Engineering
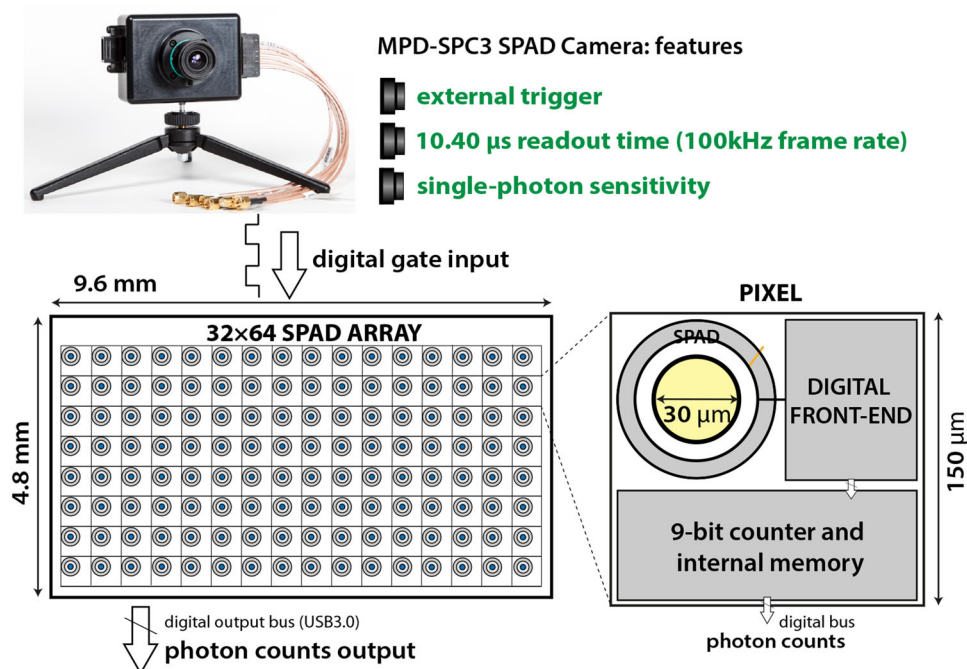Massachusetts Institute of Technology
Cambridge, MA 02139, USA
F. Madonini, F. Villa
Dipartimento di Elettronica
Informazione e Bioingegneria (DEIB)
Politecnico di Milano
Piazza Leonardo da Vinci 32, Milano 20133, Italy
B. Li, J. Xiang, P. Cappellaro
Department of Physics
Massachusetts Institute of Technology
Cambridge, MA 02139, USA

## 1. Introduction

The second quantum revolution describes all those new technologies that are enabled by the use of quantum mechanics, not only to describe the physical world, but to address, control, and detect individual quantum systems. For example, observing the behavior of individual atoms or photons enables the realization of phenomena such as quantum superposition and entanglement.[1] Nowadays, innovation is pushed in four main directions: quantum communication,[2] to transmit data more securely; quantum simulation,[3] to reproduce physical dynamics in well-controlled systems; quantum computation,[4] to speed up computations; and quantum sensing,[5] to improve measurement performance. Despite great advances, it is still challenging to achieve high-fidelity control of scalable and low-noise quantum systems.[6,7]

Just in the field of measurement, the need to address single quantum particles, rather than a macroscopic sample, requires detectors with high sensitivity (e.g., single-photon sensitivity for optical measurements).[8,9] Moreover, to scale up quantum systems for more powerful quantum information processing, it is desirable to achieve the simultaneous measurement of a larger number of quantum particles. Exemplary application scenarios include wide-field quantum sensing with solid-state spins,[10] large-scale quantum computation with Rydberg atom arrays,[9] and quantum simulation with optical lattices.[11] In addition, quantum error correction requires fast and high-fidelity measurements[12] to enable feedback on the quantum platforms based on the detected results.

Single-photon avalanche diodes (SPADs) integrated in CMOS technologies are widely used today to detect single photons, providing good overall performance with the typical advantages of microelectronic technologies, such as reliability, robustness, and compactness. Their relatively high photo-detection efficiency (PDE), along with the digital-like output (every time at least a photon is absorbed) and the absence of readout noise, makes them an arguably suitable choice for applications requiring single-photon counting or time-of-flight (TOF) evaluation. In particular, SPADs are well suited to the realization of large-format arrays for imaging applications since they allow single-photon sensitivity together with high frame rates and spatial resolution.[13] CMOS Active Pixel Sensors (APS) are high-speed devices, but they do

**ADVANCED**
**SCIENCE NEWS**
www.advancedsciencenews.com

**ADVANCED**
**QUANTUM**
**TECHNOLOGIES**
www.advquantumtech.com

**Figure 1.** MPD-SPC3 SPAD camera.

not perform internal amplification, thus suffering from low sensitivity. Electron-multiplying charged coupled devices (EMCCD) and intensified CCDs (ICCD), although having high sensitivity and possibly millions of pixels, are bulkier, slower, and more expensive than SPAD arrays.[14]

In this work, we present the development of an advanced detection system based on the MPD-SPC3 SPAD camera,[15,16] targeting light extraction from single photon emitters that can be used as quantum sensors. In comparison to state-of-the-art photon detection such as single-pixel commercial photodiodes, or spatially resolved CCD cameras in case of bulk measurements, our work is the first integration of an array of SPADs with an ensemble of nitrogen-vacancy (NV) centers in diamond, providing micrometer-scale spatial resolution and fast measurement rate (100 kHz). We build an optical microscope setup with flexible magnification factors to map the top layer of a bulk diamond to the 64 × 32 array of SPAD pixels. We achieve efficient transmission and processing of the fast-generating (> 10 Mbps) SPAD data. We benchmark our new system by demonstrating proof-of-principle examples of sensing AC and DC magnetic field, temperature, strain, local spin density, and charge dynamics with the NV ensemble. Its quantum applications for broader solid-state and atom array platforms are discussed in the outlook.

## 2. MPD-SPC3 SPAD Camera

A SPAD is a p–n junction that is reverse-biased well above its breakdown voltage.[17] Under this operating condition, the absorption of a single photon generates an electron–hole pair, which is accelerated by the high electric field across the junction. The energy of the charge carriers is eventually sufficient to trigger a macroscopic avalanche current of few milliamperes through the device. The SPAD front-end electronics, namely the

quenching circuit, can be integrated on the same silicon chip. The quenching circuit senses the avalanche current, quenches it, and resets the SPAD to its initial state. The avalanche is quenched by decreasing the voltage across the SPAD junction below breakdown for an adjustable time (hold-off), that ranges from few nanoseconds to few hundreds of nanoseconds. The SPAD bias voltage is then restored to the initial state, and thus it is ready to detect the next photon. The total time required to restore the initial state of the SPAD after the detection of a photon is named dead time. During the dead time, no photons can be detected. Due to the dead time, the SPAD has a linear working range (i.e., the number of detection events within a defined time period ($T$) depends linearly on the illumination intensity) only at low or moderate photon fluxes. At large photon fluxes, the number of detected photons deviates from linearity and saturates to a constant value, which is the reciprocal of the dead time. The measurement of light signals by a SPAD has several advantages concerning the signal-to-noise ratio. No analog measurement of voltage or current is needed, since the detector acts like a digital "Geiger-like" counter. It follows that no electronic noise is added by analog-to-digital converters or amplifiers while measuring the signal. Additionally, the detector is less sensitive to electromagnetic interference or electrical noise generated by external equipment, differently from CCDs.

The "MPD-SPC3"[15] as shown in **Figure 1** is a multipurpose single-photon counting image sensor, based on a 0.35 μm, 64 × 32 SPAD pixel array. Each smart pixel comprises a very low noise (100 cps) round SPAD with 30 μm active area diameter, a low area occupation analog quenching circuit, and digital processing electronics. The quenching front-end provides a digital pulse to the following counter block every time at least a photon impinges on it. Three 9-bit linear feedback shift register (LFSR) counters are employed to deliver 2D intensity information through

**ADVANCED**
**SCIENCE NEWS**
www.advancedsciencenews.com

**ADVANCED**
**QUANTUM**
**TECHNOLOGIES**
www.advquantumtech.com

photon counting in either free-running (down to 10-μs integration time) or time-gated mode. Free-running is the default operation and consists in continuously counting all SPAD pulses without any temporal filtering. Conversely, in time-gated mode, each of the three integrated binary counters is enabled only inside a user-defined temporal window (gate signal). The LFSR topology grants high-speed operation and low area occupation. Three in-pixel memory registers store the content of the respective counter, simultaneously for the whole array, thus allowing global shutter operation. The array readout time is proportional to the number of counters in use. In case a single counter per pixel is used, this time is equal to the time needed to read the 2048 pixels, which is 10.40-μs. The devised pixel has a pitch of 150 μm and a fill factor of 3.14%. For imaging applications, microlenses can improve the fill-factor to about 78%. The SPAD camera features high photon-detection probability (PDP) in the visible and near-UV spectral region with a peak of almost 50% at 410 nm. The minimum dead time is 50 ns, ensuring a maximum count rate of 20 Mcps. The dark count rate, that is, the rate of avalanches not caused by photon detection and mainly related to thermal carrier generation, is very low even at room temperature (100 cps per pixel).

## 3. Sensor Setup Design with Flexible Control and Readout Options

NV centers in diamond have been one of the most promising solid-state platforms for quantum sensing,[5] with optical initialization and readout of the spin state, room-temperature operational condition, and nanoscale spatial resolution. Its capabilities of sensing electromagnetic signals,[18–20] temperature,[21] strain/stress,[22] spin density,[23] charge environment[24] have been demonstrated in recent years. To further improve the readout efficiency and perform simultaneous measurement of different spatial locations, wide-field quantum sensing techniques have also been developed,[10] where a microscope objective is used to map out the spatial information, and a camera with multiple pixels is used for imaging a large number of pixels. In this section, we introduce the details of our setup design, highlighting flexible control, and readout options tailored for different application scenarios.

### 3.1. Sample Mounting, Magnetic Field, and Microwave Control

The foundational element in an NV sensing experiment is the diamond host itself. Tailoring the diamond growth recipe is vital to obtain the desired amount of NV defects while controlling the concentration of other paramagnetic centers. The diamond itself is then mounted to allow for easy access by a 532-nm excitation laser, and for collection of the resulting NV fluorescence. The diamond mount is designed to minimize thermal gradients, vibrational noise, and additional strain induced by any adhesive applied to the diamond. In our setup, the diamond is mounted over a hole of diameter ≈ 1 mm on a printed circuit board (PCB) with the conducting surface layer finished by immersion gold. The thickness of the PCB is chosen as 0.4 mm (much thinner than the typical PCB thickness of around 1.6 mm) to allow more

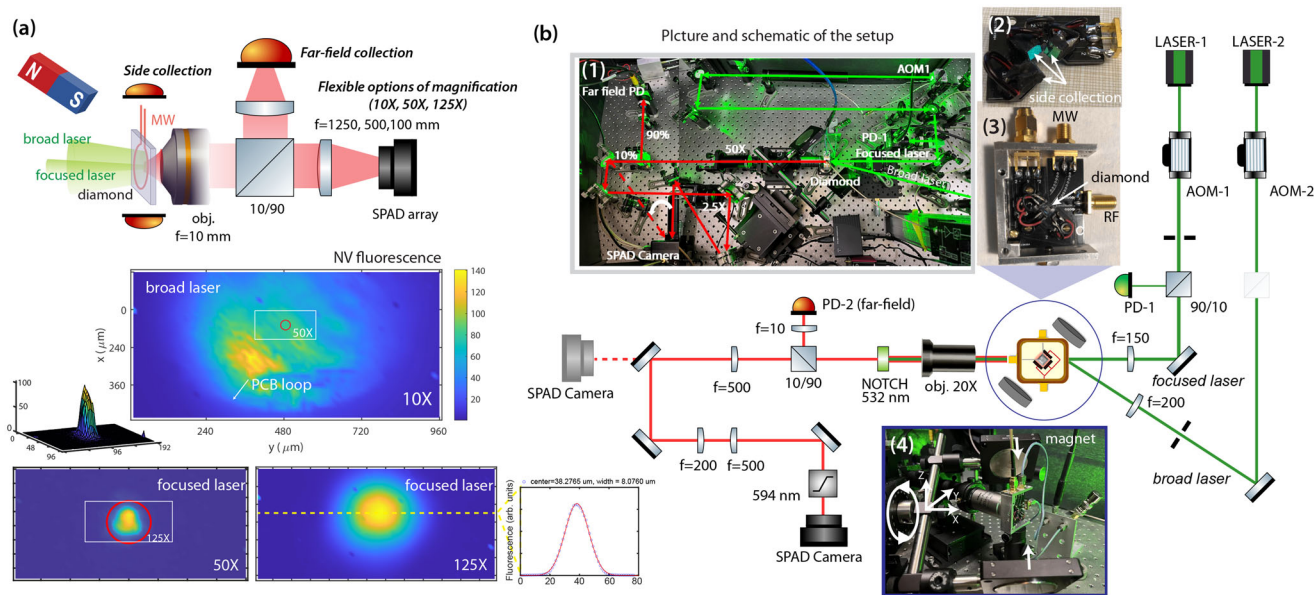photon collection via the objective mounted on the backside of the PCB board.

For NV experiments not operating at zero-field conditions, a bias magnetic field is applied to break the degeneracy of the two spin states $|m_s = \pm 1\rangle$ and spectrally distinguish the $|m_s = 0\rangle \leftrightarrow |m_s = +1\rangle$ and $|m_s = 0\rangle \leftrightarrow |m_s = -1\rangle$ transitions. We use a pair of permanent magnets mounted on a stage with $x - y - z$ translation freedom and rotation freedom. The distance between the two magnets can also be freely adjusted (shown in the inset (4) of **Figure 2**b).

One typical NV sensing method is to scan the frequency of an applied microwave field to find the NV resonance condition, which changes depending on the magnetic field to be detected. Applying resonant microwaves then allows the realization of more complicated and precise sensing protocols. Typically, a wire loop is constructed by shorting a coaxial cable, which is placed near the NV interrogation region. A microwave generator then generates a field, which is amplified and sent to the wire to drive the NV transitions. Other microwave delivery schemes include using a waveguide fabricated directly on the surface of the diamond, which however lacks convenience for sample change. In our case, the PCB holding the diamond also hosts the microwave wire loop, formed from the end of a shorted coaxial cable. The diamond is mounted such that the NV layer (usually near one of the surfaces of the diamond) is facing toward the loop (actually touching the loop) to maximize the microwave power delivered to the NV ensemble.

### 3.2. Multiple Laser Beam Settings

Optical excitation is necessary to polarize the NV center to the $|m_s = 0\rangle$ state.[25] For typical single-NV or small-ensemble volume experiments based on a confocal setup design, a microscope objective is used to both apply the optical excitation beam and detect the fluorescence signal. When applying the excitation beam, the diamond is placed at the output of the microscope objective, allowing only NVs in the diffraction-limited spot (usually 200 nm to 1 μm, depending on the numerical aperture and laser wavelength) to be optically addressed by the laser. For wide-field imaging applications, we use the microscope objective only for fluorescence detection and apply a broad laser beam from the opposite side.

To allow higher experiment flexibility such as the sensing of charge dynamics, we include two different green (532 nm) laser beams. Indeed, in standard setups, the optical readout of the NVs is performed with the same laser used for optical polarization. The use of two lasers allows the excitation and detection to be more flexible. For example, by creating a beam with a narrower focus and a higher power density and a second, broader beam with a smaller power density, we can explore charge dynamics by tuning the local electron and hole density using the ionization and recombination process of the NV center.[26] The focused beam can be used for local charge states and electron/hole density control, while the broad beam can be used for a homogeneous readout on the entire area. Besides focused-broad beam settings, more scenarios can be easily implemented such as making the two beams both focused on two different locations.

**ADVANCED
SCIENCE NEWS**

www.advancedsciencenews.com

**ADVANCED
QUANTUM
TECHNOLOGIES**

www.advquantumtech.com

**Figure 2.** Experimental setup design. a) Simplified schematic of the setup design. The NV fluorescence measured under different magnification factors and laser settings are plotted. The focused laser beam size is characterized by plotting a line cut of the NV fluorescence imaging (inset). The 3D surface plot shows the measured NV fluorescence intensity under the focused laser beam illumination. b) Setup design and pictures. Two laser beams with flexible sizes on the diamond are gated by two AOMs. The maximum magnification factor of 125 is realized by two magnification steps (50× and 2.5×). The second step can be bypassed when only small magnification factors are needed.

We use beamsplitters together with half-wave plates to generate the two laser beams from the same laser source (SPROUT-G, 5 W). Each of them is independently gated by an acousto-optic modulator (AOM) in combination with an iris. The gating signals are provided by a pulse blaster (PulseBlasterESR-PRO 500) such that the laser can be turned on and off in experimental sequences. The optical paths shown in Figure 2b are designed to have LASER-1 very focused (30 µm-diameter) and LASER-2 broader (>200 µm-diameter).

### 3.3. Multiple Detection Options

#### 3.3.1. Side Collection and Far-Field Collection

Due to total internal reflection, for a bulk diamond plate with a thin thickness in the $z$-direction, more fluorescence light actually emerges from the side edges.[27] We devise a separate piece of PCB based on the idea of ref. [27], where three photodiodes (area 2 mm × 2 mm each, with attached a thin customized long-pass filter to block the excitation light) are placed on the side of the diamond (shown in the inset of Figure 2b). The instantaneous current of the photodiode (Hamamatsu S8729) is sampled and converted to voltage signal by a variable gain high-speed (200 MHz) current converter (DHPCA-100), which is then measured by a National Instrument data acquisition card (NI PCI-6281) gated by the pulse blaster. With a high signal-to-noise ratio and data acquisition efficiency, the side collection detection option was mostly used in our previous work where no spatial information was required.[28,29]
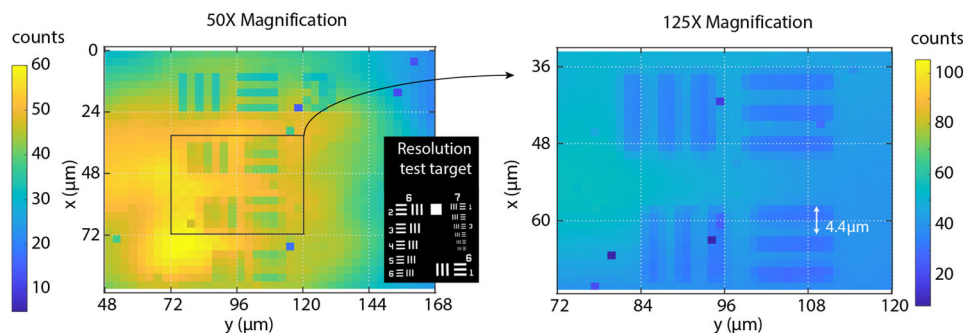
Even though separate pieces of PCB are used for delivering microwaves and performing data collection as shown in the insets

(2,3) of Figure 2b, the side collection suffers from circuit interference due to microwave driving and laser heating. Thus, we also use a microscope objective to collect fluorescence from the backside of the PCB. The fluorescence signal is then sent to a variable gain photodiode (PBA36A). Both collection options can be operated simultaneously, providing better fluorescence collection efficiency.

To cancel the noise due to laser intensity fluctuation, we add a 10/90 beamsplitter to sample a fraction of the intensity of either of the two laser sources. The signal is then collected by a separate photodiode (PBA36A), which is useful to characterize and compensate for the laser noise. When far-field detection is used for data collection, we can use a balanced photodiode (such as PDB230A) to perform the laser noise cancellation with even better performance.

#### 3.3.2. SPAD Array with Multiple Magnification Factors

The wide-field fluorescence collection with MPD-SPC3 camera shares the same objective (N20X-PF - 20X Nikon Plan Fluorite Imaging Objective, 0.50 NA, 2.1 mm, 10 mm effective focal length)) as the far-field collection path. To match the SPC3 camera's 150µm pixel size with the desired spatial resolution ≈ 1µm, and ensure the off-axis light can be well captured by the lenses, we design a two-stage magnification process to achieve the magnification factor of 125. As depicted in Figure 2b, a first 50× factor is reached with an achromatic lens with a 500 mm focal length. A second 2.5× magnification factor is obtained with a couple of achromatic lenses with focal lengths of 200 and 500 mm. As a standard rule, mirrors were used to gain centimeter distances on the limited optical table. In particular, flip mounts were

**ADVANCED
SCIENCE NEWS**
www.advancedsciencenews.com

**ADVANCED
QUANTUM
TECHNOLOGIES**
www.advquantumtech.com

**Figure 3.** Spatial resolution. Spatial resolution measurement with a resolution test target (Thorlabs USAF 1951 R3L1S4P). The fluorescence of an NV ensemble of a diamond sample is used as the light source.

exploited for mirrors in order to potentially bypass the second magnification and keep only the first 50× factor indicated by the white arrow in the insets (1) of Figure 2b. Moreover, by changing the second lens focal length, and consistently moving the SPAD camera, it is straightforward to reach a different magnification value (such as 10×, employed in the experiments described below). Such interchangeable optics ensures a compact and flexible sensor for spatially resolved images of NV quantum sensor. In practical experiments, high-throughput measurements allow a fast pre-screening of the diamond in a much larger spatial range with a smaller magnification factor before performing finer experiments with larger magnification factors.

The diamond emits red fluorescence but also a large amount of the green laser passes through it. A notch filter (532 and 1064 nm) is placed after the objective to filter out the green light. Moreover, a long-pass filter (594 nm) on the SPAD camera eliminates the remaining green light in favor of red fluorescence.

We experimentally demonstrate the spatial resolution using a resolution test target as shown in **Figure 3**. A bulk diamond with an NV ensemble is used as the light source, which is glued to the resolution test target (with the NV layer facing towards the target), and a broad green laser beam of about 100 μm diameter is applied to the group element seven of the test target. The images of the test target with 50× and 125× magnification options are shown in Figure 3. A spatial resolution below 2 μm is thus demonstrated.

The integration time of the SPAD camera is set by its control interface on the experimental computer, while the timing of the data acquisition is gated by the same pulse blaster, which is programmed in each experiment to synchronize and trigger different electronic components including laser excitation (through AOMs), microwave radiation, and photodiodes' measurement (through the data acquisition card). The quickly generated SPAD data is transmitted to the computer through a USB 3.0 port. Efficient data processing, especially for data size of tens of gigabytes, can be achieved with the memory-mapping method based on MATLAB.

## 4. Applications in Quantum Sensing
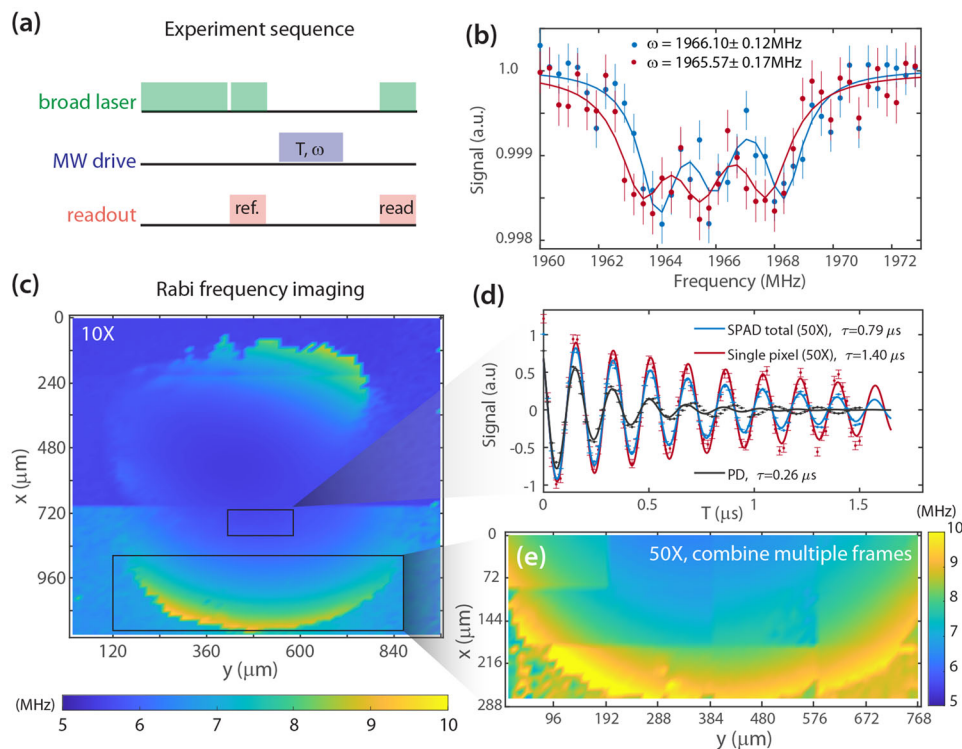
### 4.1. Microwave Imaging by Rabi Magnetometry

To sense an oscillating magnetic field with a frequency $\omega_s$, one can use the static bias field to tune the NV single quantum (SQ) transition frequency $\omega_0 = D \pm \gamma_e B_z$ to this frequency (here $\gamma_e = (2\pi)2.8$ MHz G$^{-1}$ is the gyromagnetic ratio, $D = (2\pi)2.87$ GHz is the zero-field splitting.) When the resonance condition is satisfied $\omega_0 = \omega_s$, the NV center, starting from an initial state $|0\rangle$, undergoes coherent oscillations between $|0\rangle$ and $|-1\rangle$ (or $|+1\rangle$) with a frequency $\Omega_s = \gamma_e B_s / \sqrt{2}$, called Rabi frequency. Experimentally, we monitor the time-dependent population $P_{|0\rangle} = (1 + \cos(\Omega_s T))/2$, from which we obtain the Rabi frequency and then the amplitude $B_s$ of the target signal (**Figure 4**a).[30]

As a demonstration of the flexibility of the designed setup, we use Rabi magnetometry to map the microwave field amplitude generated by the loop structure on our PCB. We use the broad laser beam to address a large area of the diamond. The measured Rabi oscillation with different collection options is shown in Figure 4d. By fitting the oscillation signal to a decaying sinusoidal $S(T) = c_0 + c \cos(\omega_s T + \phi)e^{-T/\tau}$, we can obtain the coherence time $T_{2\rho} = \tau$ and Rabi frequency $\omega_s$. The single-pixel measurement has a longer coherence time (1.40 μs) than the average signal over all pixels (0.79 μs, both measured under a 50× magnification factor). Similarly, the far-field photodiode measurement gives the shortest coherence time (only 0.26 μs) shown by the black data points in Figure 4d because the signal is collected over a much larger spatial area (covering almost the whole area within the loop). In Figure 4c, we choose the 10× magnification option to image the microwave amplitude in a large field of view. We combine three frames measured under different γ stage positions and show the microwave amplitude distribution generated by the loop. The Rabi frequency near the proximity of the loop is close to 10 MHz, while in the central region it is quite homogeneous and is close to 5 MHz. In Figure 4e, we combine twelve frames to measure a large region using the 50× magnification option, which images the gradient near the edge of the loop.

We note that the discontinuity of the image at the edge of each individual frame is due to different frequency detuning $\omega_0 - \omega_s$ when measuring different frames. The effective Rabi frequency is then modified to $\Omega_{\text{eff}} = \sqrt{\Omega_s^2 + (\omega_0 - \omega_s)^2}$. These frequency mismatches may be induced by gradients of the magnetic field, temperature, or strain. The characterization of these gradients will be introduced shortly in the following sub-sections.

Our results demonstrate the capability of our setup in imaging microwaves with Rabi magnetometry. The coherence time $T_{2\rho}$ of Rabi oscillation strongly depends on the spatial range of the signal collection, which validates the decay mechanism due to

**ADVANCED
SCIENCE NEWS**

www.advancedsciencenews.com

**ADVANCED
QUANTUM
TECHNOLOGIES**

www.advquantumtech.com

**Figure 4.** Microwave imaging. a) Experimental sequence for Rabi oscillation measurements. b) ODMR measurement of two locations separated by 12 μm. A small bar magnet is placed 1 cm away from the diamond to apply the additional magnetic gradient. 4-by-4 pixel grouping under the 50× magnification option is used to improve the SNR. c) Imaging of Rabi frequency using the 10× magnification option of the optical path. Three frames with different $x$ stage positions are combined together. 200 000 experimental repetitions are used to improve the SNR. The same repetition number applies to other SPAD measurements in this figure. d) Comparison of Rabi oscillation data collected by the far-field photodiode, individual and total pixels of the SPAD camera under the 50× magnification option. e) Rabi imaging with the 50× magnification option by combining 12 frames.

spatial inhomogeneity of the microwave field proposed in our previous work.[28] In comparison to photodiode measurement giving rise to short coherence time, the SPAD measurement combines both benefits of long coherence time and spatially resolved information.
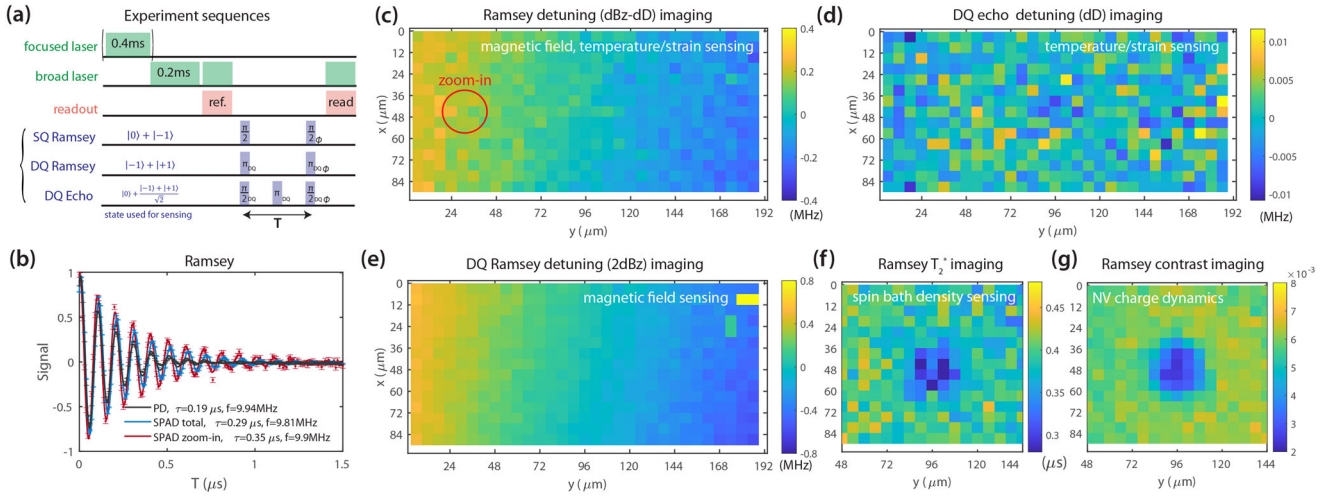
### 4.2. Magnetic Field Imaging by Ramsey Magnetometry

To sense a static magnetic field, we can apply an initial $\pi/2$ pulse to prepare the spin state in the SQ superposition state $(|0\rangle + |-1\rangle)/\sqrt{2}$. After an evolution time $T$, a relative phase $\varphi(T) = (dD - \gamma_e dB_z)T$ is accumulated, before a final $\pi/2$ pulse and projective optical measurement realizes a population readout. Here $dD, dB_z$ are shifts of the zero-field splitting and the static magnetic field in different spatial locations with respect to their mean values calibrated by an experiment summing up the whole area. Usually, the final $\pi/2$ pulse is realized with a time-dependent phase $\phi = \nu T$ with respect to the first $\pi/2$ pulse, which adds an additional oscillation at a frequency $\nu$ to the signal to better visualize the spin coherence behavior. The sequence is shown in **Figure 5**a. When the temperature and strain are constant and homogeneous, SQ Ramsey magnetometry can be used to measure the static magnetic field $dB_z$.

We choose the 50× magnification option (same for all experiments below) to perform wide-field imaging of the magnetic field. The experimental results are shown in Figure 5c, where a clear gradient along the $y$ direction can be seen. The deduced magnetic field change from $y = 0$ to $y = 192$ μm is about 0.286 G. Since the NV transition frequency inhomogeneity due to the magnetic field gradient is much smaller than the Rabi frequency, such a gradient would not affect the Rabi imaging measurement (Figure 4) too much. Moreover, the characterized gradient may be used to improve microwave imaging. In Figure 5b we compare again the photodiode and SPAD measurements. The shortest Ramsey coherence time $T_2^* \approx 0.19$ μs is observed in the photodiode measurement, while the average signal of the SPAD image gives 0.29 μs and the total signal of a small group of pixels shown by the red circle in (c) gives a longer 0.35 μs. We note that the gradient of temperature or strain that leads to variation in $D$ may also introduce a NV resonance frequency gradient. The magnetic field, temperature, and strain gradients, as well as the intrinsic spin bath with magnetic dipolar interactions, contribute to the decay of the Ramsey signal.[31,32]

To further validate that the measured spatial gradient is given by the magnetic field $dB_z$ instead of the shift in zero-field splitting $dD$, we introduce the DQ Ramsey magnetometry, which uses an initial DQ superposition state $(|+1\rangle + |-1\rangle)/\sqrt{2}$ prepared by simultaneously applying resonance microwave driving to both of the two SQ transitions. The accumulated relative phase at time $T$ is then $\varphi(T) = 2\gamma_e dB_z T$, which is twice larger than the SQ

**2300046 (6 of 10)**

**ADVANCED
SCIENCE NEWS**

www.advancedsciencenews.com

**ADVANCED
QUANTUM
TECHNOLOGIES**

www.advquantumtech.com

**Figure 5.** Quantum sensing with wide-field imaging. a) Experimental sequence for SQ Ramsey, DQ Ramsey, DQ echo measurements. b) SQ Ramsey experiments with different photon collection options and spatial ranges. The SPAD 64×32 pixels are grouped to 32×16 pixels to improve the signal-to-noise ratio (same for all the other data in this figure). c) The detuning frequency imaging of SQ Ramsey experiments. The mean fitting uncertainty of the detuning value is 0.067 MHz. 120 000 experimental repetitions are used to improve the SNR. The same repetition number applies to the SQ Ramsey measurements in other plots. d) The detuning frequency imaging of DQ echo experiments. The mean fitting uncertainty of the detuning value is 0.007 MHz. 160 000 experimental repetitions are used to improve the SNR. e) The detuning frequency imaging of DQ Ramsey experiments. The abnormal spots in the upper right corner are due to the fitting failure in the data processing. The mean fitting uncertainty of the detuning value is 0.095 MHz. 160 000 experimental repetitions are used to improve the SNR. f) The coherence time imaging of SQ Ramsey experiments with the focused laser beam illuminated as shown in sequence (a). The mean fitting uncertainty of the $T_2^*$ value is 0.045 µs. g) The signal contrast imaging of SQ Ramsey experiments with the focused laser beam illuminated. The mean fitting uncertainty of the contrast value is 0.0007.

Ramsey case when $dD = 0$. The DQ Ramsey measurement is independent of the frequency shift in $D$, thus excluding the potential contribution from temperature, strain, or electric field, which mainly affects the NV transition frequency by changing the value of $D$. The experimental results are shown in Figure 5e, which are consistent with the image in (c) (the gradient of the Ramsey detuning frequency in (e) is twice larger than the SQ measurement in (c)).

The sensitivity of our SPAD setup can be roughly estimated using the fitting uncertainty of the detuning $\delta\omega = 0.067$ MHz for 4-pixels DQ Ramsey measurement, such that the sensitivity per pixel is $\eta = \frac{\delta\omega}{2\gamma_e}\sqrt{N \times 4 \times (t + t_d)} = 0.58$ mT $(\sqrt{\text{Hz}})^{-1}$. Here $N = 160\,000 \times 151$ is the total number of experiments, $t_d$ is the sequence deadtime and $t + t_d \approx 0.3$ ms. In Figure 4b, we also test the capability of our setup in resolving magnetic field gradient, where we show that a $0.53 \pm 0.21$ MHz ODMR shifts (corresponding to 0.2 G) over a distance of 12 µm can be resolved.

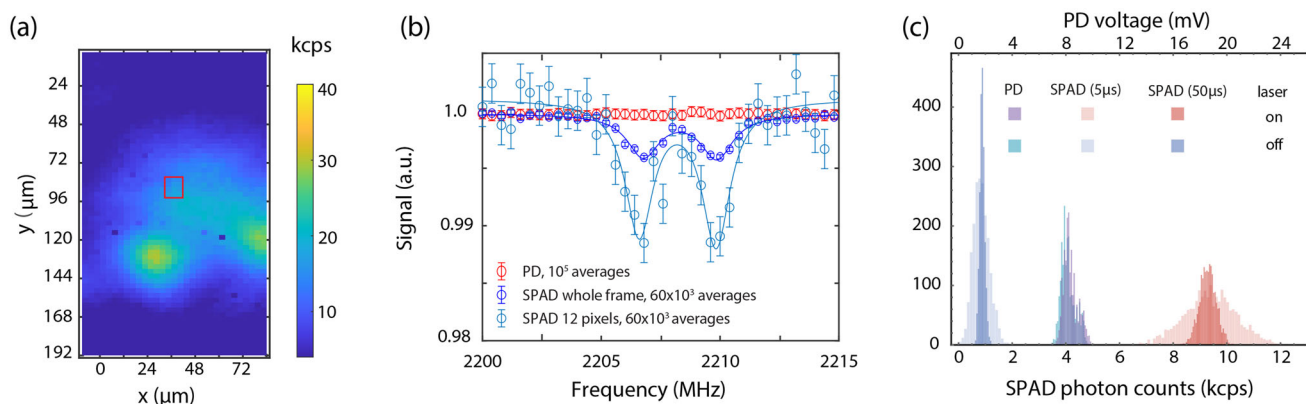### 4.3. Temperature and Strain Sensing by Double-Quantum Echo (or D-Ramsey)

To sense the shift in zero-field splitting $D$, the magnetic field coupling term needs to be canceled by the double-quantum spin echo, which adds a double-quantum $\pi$ pulse in the middle of the Ramsey sequence. The method, also called D-Ramsey, has been used in measuring temperature[33,34] and crystal strain.[35] Different from most previous work where the SQ superposition state is used as the initial state, here we use a superposition state $[|0\rangle + (|+1\rangle + |-1\rangle)/\sqrt{2}]/\sqrt{2}$, which can be prepared by simultaneously applying resonance microwave driving to both of the two

SQ transitions for a duration (half the duration of the initial pulse in DQ Ramsey, which prepares the state $|+1\rangle + |-1\rangle$), or by composite SQ pulses (a $\pi/2$ pulse applied to one SQ transition, before a $2\cos^{-1}\sqrt{2/3}$ pulse applied to the other SQ transition). A DQ $\pi$ pulse is applied in the middle of the free evolution, which is composed of three SQ $\pi$ pulses applied to the $|0\rangle \leftrightarrow |-1\rangle$, $|0\rangle \leftrightarrow |+1\rangle$, $|0\rangle \leftrightarrow |-1\rangle$ transitions.

The measured frequency shift $dD$, plotted in Figure 5d shows quite small values (less than 0.01 MHz) in the whole image. The result demonstrates the homogeneous spatial distribution of both the temperature (<0.15 K) and strain (<1 ppm).

### 4.4. Spin Bath Characterization and Charge Dynamics

When analyzing the Ramsey decoherence time of NV centers within a single pixel (or a small group of pixels) such that the magnetic field, temperature, or strain inhomogeneity is small, the dominant noise is then given by the surrounding spins which are coupled to the NV spin through magnetic dipolar interaction. A simple dimensional analysis predicts that the decay rate $1/T_2^*$ should be proportional to the local spin density, as recently analyzed.[23,36] Thus, characterizing the Ramsey decoherence provides a probe of the local spin density. To create a spin density gradient in our system, we use the focused beam with a large power density to quickly drive the cycling transition between the two charge states NV$^-$ and NV$^0$,[26,37] which continuously pump electrons from the valence band to the conduction band. The generated electrons then combine with positively charged nitrogen defects (without spin) and convert them to neutrally charged nitrogen defects (P1 center, spin 1/2),[38] which

**ADVANCED**
**SCIENCE NEWS**
www.advancedsciencenews.com

**ADVANCED**
**QUANTUM**
**TECHNOLOGIES**
www.advquantumtech.com

**Figure 6.** Test on a sparse sample. a) NV density and laser beam size imaging. A 30 mW 532 nm green laser is slightly defocused to make a beam with about 100 μm diameter. b) ODMR experiments measured by far-field photodiode, SPAD whole frame, SPAD 12 pixels. No beam-splitter or ND filter is used such that all the fluorescence collected by the objective is sent to either the photodiode or the SPAD camera. The 12 pixels grouping used in the plot is shown by the red box in (a). c) Histogram of average single pixel photon counts for single frame measurements with 5,50 μs integration times with the SPAD array, versus voltage from the far-field photodiode (PD) for single measurements.

shortens the Ramsey coherence time. The experimental results are shown in Figure 5f, where the Ramsey coherence time in the central region is shorter than the outer region, indicating a larger spin density in the central region. In Figure 5g, we show the signal contrast of Ramsey measurement at short times. The region illuminated by the focused laser beam shows a much smaller signal contrast. The contrast decrease under laser illumination is due to the ionization of $NV^-$, which decreases the number of NV centers used for quantum sensing (the $NV^0$ charge state also emits red fluorescence under the green laser, but it cannot be used for quantum sensing due to a different energy structure, so it does not provide any signal contrast).

### 4.5. Performance Test on a Diamond with Sparse NV Centers

To test our camera for sparse emitters, we use a diamond sample grown with nitrogen-15 and NV centers are concentrated in a 1 μm thin layer below the diamond surface. The estimated NV density is lower than 10 ppb. We illuminate the diamond using a 100 μm diameter green laser beam such that the beam size is similar to the frame size as shown in **Figure 6**a. Due to the low fluorescence intensity, we send the signal collected by the objective either to the camera or to the far-field photodiode. The ODMR experiments measured by the SPAD and the photodiode are shown in Figure 6b, which show the sensitivity advantage of our camera in sensing sparse emitters than photodiodes. We note that the contrast of the whole frame is different from the contrast of a small group of pixels. Factors that affect the contrast include spin initialization/readout timescale, charge dynamics, etc. which depend on the laser intensity and illumination sequence. The signal and background noise of the two collection options are shown in Figure 6c, which also indicates better performance of the SPAD array.

### 5. Discussions and Outlook

In this work, we report the application of single photon avalanche diode arrays to quantum information processing applications.

The SPAD array features a fast frame rate, single photon sensitivity, and external gated control, which can be synchronized with state-of-the-art quantum devices to boost their measurement performance. Using a quantum sensor based on solid-state spins as the demonstrating platform, we integrate the SPAD array with a microscope objective to build a fast wide-field quantum imaging setup. With flexible photon collection options, our setup can either be optimized to collect the total fluorescence signal or be tailored to do wide-field quantum imaging with single-photon sensitivity. We use a bulk diamond sample with an NV ensemble to show the capability of our setup in sensing dc and ac magnetic fields, temperature, strain, spin density, and charge dynamics.

We note that our proof-of-principle demonstration of various quantum sensing applications is based on an NV ensemble sample with ≈10 ppm nitrogen density and ≈0.4 ppm $NV^-$ density, which provides a much larger fluorescence intensity than a sample with sparse single NV centers (where the separation of NV is larger than the resolution of the microscope). As a result, we need to attenuate the fluorescence signal to match the photon collection rate of the SPAD camera (at most 1 photon/50 ns, corresponding to 20 M counts $s^{-1}$), and only about 1–3% of the photons collected by the microscope are sent into the camera. This actually allows more than 90% of the signal to be simultaneously collected by the photodiodes, providing both high sensitivity to the average signal and spatial information on the distribution of the target quantity. When measuring sparse emitters with low photon count rates, to optimize the SPAD collection efficiency all fluorescence signal should be sent to the camera to fully utilize the single-photon sensitivity. To further improve the SPAD collection efficiency, microlenses can be used to increase the effective pixel fill factor to about 78%, and other collection techniques such as solid immersion lenses (SIL) and light pipes/guides can also be integrated to improve the collection efficiency.[30,39–43]

With a fast frame rate, our setup is suitable for studying dynamical processes such as the charge transport phenomena in diamond.[26,37,44] Although typical wide-field sensing setups based on CCD-type cameras usually have more pixels and can count larger fluorescence signals, they cannot reach single

**ADVANCED
SCIENCE NEWS**

www.advancedsciencenews.com

**ADVANCED
QUANTUM
TECHNOLOGIES**

www.advquantumtech.com

photon sensitivity and their frame rate is usually ranging from Hz to kHz. Actually, if both the photon sensitivity and frame rate of the CCD camera can be improved to be similar to our camera, the storage and transmission of the extremely fast-growing data size will be the main challenge in building those devices.

With single-photon sensitivity, our setup is an ideal platform to image an array of single-photon emitters (with a typical separation distance of $\approx 1.1\mu m$), which can be created by ion implantation,[45] or sparse NV ensembles (<100 ppb concentration). Using the typical single NV photon collection rate of about 50k counts $s^{-1}$ under NA = 1.3 to estimate, our setup (NA = 0.5) can measure up to around 1000 NV centers within the diffraction-limited detection volume, which corresponds to 25 ppb nitrogen-vacancy concentration if we assume 100 nm NV layer thickness. Due to photon shot noise larger emitter ensembles are generally giving a better sensitivity, single or sparse emitters are advantageous for achieving high spatial resolution though the signal readout is less efficient and a large number of averages are usually needed. Moreover, the readout fidelity of single emitters can be improved to more than 95% with spin-to-charge conversion,[46] ancilla-assisted repetitive readout,[47] resonant optical excitation techniques.[48]

Current state-of-the-art wide-field sensors based on dense spin ensembles are usually built with CMOS cameras. To achieve a fast frame rate matching the optimized sensing sequence while maintaining reasonable data size (only keeping the averaged signal), various modulation/demodulation techniques are developed such as parallel lock-in measurements,[49–51] optical choppers,[52] optical streaking techniques.[53] For conventional sensing tasks with high-density ensembles, these sensors are expected to have better sensitivity performances. However, it remains difficult for these setups to efficiently measure fast dynamics (e.g., tens of kHz) or image single/sparse emitters for high spatial resolution. In contrast, the wide-field sensors based on SPAD arrays show advantages by directly achieving a high frame rate up to 100 kHz with single-photon sensitivity. Besides nanoscale quantum sensing, applications include feedback or adaptive control based on multiple different measurements in a single sequence,[54,55] spatial and temporal correlation measurements such as covariance magnetometry,[56] as well as characterization of fast dynamical processes such as defect ionization and charge transport dynamics in solids.[26]

Our setup can be applied to other quantum platforms such as atom arrays trapped in optical tweezers,[9] which have emerged as a promising system for large-scale quantum computation and quantum simulation. However, one of the major limitations of these platforms is the slow signal readout rate slower than the qubit decoherence, preventing the applications of potential quantum error correction codes. Integrating our SPAD array with the atom array provides a potential solution to these problems.

## Conflict of Interest

The authors declare no conflict of interest.

## Author Contributions

G.W., F.M., and B.L. contributed equally to this work. G.W. and P.C. conceived the idea. G.W. and F.M. designed and built the setup with assistance from B.L., C.L., and J.X. G.W., F.M., and B.L. wrote the control interface and data processing software. G.W. and F.M. implemented quantum sensing experiments and analyzed the data. All authors discussed the results.

## Data Availability Statement

The data that support the findings of this study are available from the corresponding author upon reasonable request.

[1] R. Horodecki, P. Horodecki, M. Horodecki, K. Horodecki, *Rev. Mod. Phys.* **2009**, *81*, 865.

[2] N. Gisin, R. Thew, *Nat. Photonics* **2007**, *1*, 165.

[3] I. M. Georgescu, S. Ashhab, F. Nori, *Rev. Mod. Phys.* **2014**, *86*, 153.

[4] M. A. Nielsen, I. L. Chuang, *Quantum Computation and Quantum Information*, 10th edition, Cambridge University Press, Cambridge **2011**.

[5] C. L. Degen, F. Reinhard, P. Cappellaro, *Rev. Mod. Phys.* **2017**, *89*, 035002.

[6] D. Suter, G. A. Álvarez, *Rev. Mod. Phys.* **2016**, *88*, 041001.

[7] D. A. Lidar, T. A. Brun, *Quantum Error Correction*, Cambridge University Press, Cambridge **2013**.

[8] G. Zhang, Y. Cheng, J.-P. Chou, A. Gali, *Appl. Phys. Rev.* **2020**, *7*, 031308.

[9] M. Saffman, T. G. Walker, K. Mølmer, *Rev. Mod. Phys.* **2010**, *82*, 2313.

[10] S. C. Scholten, A. J. Healey, I. O. Robertson, G. J. Abrahams, D. A. Broadway, J.-P. Tetienne, *J. Appl. Phys.* **2021**, *130*, 150902.

[11] C. Gross, I. Bloch, *Science* **2017**, *357*, 995.

[12] W. Xu, A. V. Venkatramani, S. H. Cantú, T. Šumarac, V. Klüsener, M. D. Lukin, V. Vuletić, *Phys. Rev. Lett.* **2021**, *127*, 050501.

[13] I. Cusini, D. Berretta, E. Conca, A. Incoronato, F. Madonini, A. A. Maurina, C. Nonne, S. Riccardo, F. Villa, *Front. Phys.* **2022**, *10*, 906671.

[14] F. Madonini, F. Severini, F. Zappa, F. Villa, *Adv. Quantum Technol.* **2021**, *4*, 2100005.

[15] D. Bronzi, F. Villa, S. Tisa, A. Tosi, F. Zappa, D. Durini, S. Weyers, W. Brockherde, *IEEE J. Sel. Top. Quantum Electron.* **2014**, *20*, 355.

[16] B. Ndagano, H. Defienne, A. Lyons, I. Starshynov, F. Villa, S. Tisa, D. Faccio, *npj Quantum Inf.* **2020**, *6*, 94.

**ADVANCED
SCIENCE NEWS**

www.advancedsciencenews.com

**ADVANCED
QUANTUM
TECHNOLOGIES**

www.advquantumtech.com

[17] I. Cusini, D. Berretta, E. Conca, A. Incoronato, F. Madonini, A. A. Maurina, C. Nonne, S. Riccardo, F. Villa, *Front. Phys.* **2022**, *10*, 906675.

[18] J. M. Taylor, P. Cappellaro, L. Childress, L. Jiang, D. Budker, P. R. Hemmer, A. Yacoby, R. Walsworth, M. D. Lukin, *Nat. Phys.* **2008**, *4*, 810.

[19] J. R. Maze, P. L. Stanwix, J. S. Hodges, S. Hong, J. M. Taylor, P. Cappellaro, L. Jiang, M. V. G. Dutt, E. Togan, A. S. Zibrov, A. Yacoby, R. L. Walsworth, M. D. Lukin, *Nature* **2008**, *455*, 644.

[20] F. Dolde, H. Fedder, M. W. Doherty, T. Nöbauer, F. Rempp, G. Balasubramanian, T. Wolf, F. Reinhard, L. C. L. Hollenberg, F. Jelezko, J. Wrachtrup, *Nat. Phys.* **2011**, *7*, 459.

[21] G. Kucsko, P. C. Maurer, N. Y. Yao, M. Kubo, H. J. Noh, P. K. Lo, H. Park, M. D. Lukin, *Nature* **2013**, *500*, 54.

[22] S. Hsieh, P. Bhattacharyya, C. Zu, T. Mittiga, T. J. Smart, F. Machado, B. Kobrin, T. O. Höhn, N. Z. Rui, M. Kamrani, S. Chatterjee, S. Choi, M. Zaletel, V. V. Struzhkin, J. E. Moore, V. I. Levitas, R. Jeanloz, N. Y. Yao, *Science* **2019**, *366*, 1349.

[23] S. Li, H. Zheng, Z. Peng, M. Kamiya, T. Niki, V. Stepanov, A. Jarmola, Y. Shimizu, S. Takahashi, A. Wickenbrock, D. Budker, *Phys. Rev. B* **2021**, *104*, 094307.

[24] S. Dhomkar, H. Jayakumar, P. R. Zangara, C. A. Meriles, *Nano Lett.* **2018**, *18*, 4046.

[25] R. Schirhagl, K. Chang, M. Loretz, C. L. Degen, *Annu. Rev. Phys. Chem.* **2014**, *65*, 83.

[26] G. Wang, C. Li, H. Tang, B. Li, F. Madonini, F. F. Alsallom, W. K. C. Sun, P. Peng, F. Villa, J. Li, P. Cappellaro, *arXiv:2302.12742*, **2023**.

[27] D. Le Sage, L. M. Pham, N. Bar-Gill, C. Belthangady, M. D. Lukin, A. Yacoby, R. L. Walsworth, *Phys. Rev. B* **2012**, *85*, 121202.

[28] G. Wang, Y.-X. Liu, P. Cappellaro, *New J. Phys.* **2020**, *22*, 123045.

[29] G. Wang, A. R. Barr, H. Tang, M. Chen, C. Li, H. Xu, J. Li, P. Cappellaro, *arXiv:2205.02790*, **2022**.

[30] S. T. Alsid, J. M. Schloss, M. H. Steinecker, J. F. Barry, A. C. Maccabe, G. Wang, P. Cappellaro, D. A. Braje, *Phys. Rev. Applied* **2022**, *19*, 054095.

[31] E. Bauch, S. Singh, J. Lee, C. A. Hart, J. M. Schloss, M. J. Turner, J. F. Barry, L. M. Pham, N. Bar-Gill, S. F. Yelin, R. L. Walsworth, *Phys. Rev. B* **2020**, *102*, 134210.

[32] E. Bauch, C. A. Hart, J. M. Schloss, M. J. Turner, J. F. Barry, P. Kehayias, S. Singh, R. L. Walsworth, *Phys. Rev. X* **2018**, *8*, 031025.

[33] D. M. Toyli, C. F. de las Casas, D. J. Christle, V. V. Dobrovitski, D. D. Awschalom, *Proc. Natl. Acad. Sci. USA* **2013**, *110*, 8417.

[34] P. Neumann, I. Jakobi, F. Dolde, C. Burk, R. Reuter, G. Waldherr, J. Honert, T. Wolf, A. Brunner, J. H. Shim, D. Suter, H. Sumiya, J. Isoya, J. Wrachtrup, *Nano Lett.* **2013**, *13*, 2738.

[35] M. C. Marshall, R. Ebadi, C. Hart, M. J. Turner, M. J. Ku, D. F. Phillips, R. L. Walsworth, *Phys. Rev. Appl.* **2022**, *17*, 024041.

[36] V. Stepanov, S. Takahashi, *Phys. Rev. B* **2016**, *94*, 024421.

[37] H. Jayakumar, J. Henshaw, S. Dhomkar, D. Pagliero, A. Laraoui, N. B. Manson, R. Albu, M. W. Doherty, C. A. Meriles, *Nat. Commun.* **2016**, *7*, 12660.

[38] A. Lozovoi, D. Daw, H. Jayakumar, C. A. Meriles, *Phys. Rev. Mater.* **2020**, *4*, 053602.

[39] R. N. Patel, T. Schröder, N. Wan, L. Li, S. L. Mouradian, E. H. Chen, D. R. Englund, *Light Sci. Appl.* **2016**, *5*, e16032.

[40] R. A. Wambold, Z. Yu, Y. Xiao, B. Bachman, G. Jaffe, S. Kolkowitz, J. T. Choy, M. A. Eriksson, R. J. Hamers, M. A. Kats, *Nanophotonics* **2021**, *10*, 393.

[41] M. Jamali, I. Gerhardt, M. Rezai, K. Frenner, H. Fedder, J. Wrachtrup, *Rev. Sci. Instrum.* **2014**, *85*, 123703.

[42] D. Wildanger, B. R. Patton, H. Schill, L. Marseglia, J. P. Hadden, S. Knauer, A. Schönle, J. G. Rarity, J. L. O'Brien, S. W. Hell, J. M. Smith, *Adv. Mater.* **2012**, *24*, OP309.

[43] V. Yurgens, J. A. Zuber, S. Flågan, M. De Luca, B. J. Shields, I. Zardo, P. Maletinsky, R. J. Warburton, T. Jakubczyk, *ACS Photonics* **2021**, *8*, 1726.

[44] A. Lozovoi, H. Jayakumar, D. Daw, G. Vizkelethy, E. Bielejec, M. W. Doherty, J. Flick, C. A. Meriles, *Nat. Electron.* **2021**, *4*, 717.

[45] J. Wang, F. Feng, J. Zhang, J. Chen, Z. Zheng, L. Guo, W. Zhang, X. Song, G. Guo, L. Fan, C. Zou, L. Lou, W. Zhu, G. Wang, *Phys. Rev. B* **2015**, *91*, 155404.

[46] Q. Zhang, Y. Guo, W. Ji, M. Wang, J. Yin, F. Kong, Y. Lin, C. Yin, F. Shi, Y. Wang, J. Du, *Nat. Commun.* **2021**, *12*, 1529.

[47] P. Neumann, J. Beck, M. Steiner, F. Rempp, H. Fedder, P. R. Hemmer, J. Wrachtrup, F. Jelezko, *Science* **2010**, *329*, 542.

[48] L. Robledo, L. Childress, H. Bernien, B. Hensen, P. F. A. Alkemade, R. Hanson, *Nature* **2011**, *477*, 574.

[49] C. A. Hart, J. M. Schloss, M. J. Turner, P. J. Scheidegger, E. Bauch, R. L. Walsworth, *Phys. Rev. Appl.* **2021**, *15*, 044020.

[50] M. A. Keppler, Z. A. Steelman, Z. N. Coker, M. Nesládek, P. R. Hemmer, V. V. Yakovlev, J. N. Bixler, *Photonics Res.* **2022**, *10*, 2147.

[51] M. Parashar, A. Bathla, D. Shishir, A. Gokhale, S. Bandyopadhyay, K. Saha, *Sci. Rep.* **2022**, *12*, 8743.

[52] L. M. Pham, D. Le Sage, P. L. Stanwix, T. K. Yeung, D. Glenn, A. Trifonov, P. Cappellaro, P. R. Hemmer, M. D. Lukin, H. Park, A. Yacoby, R. L. Walsworth, *New J. Phys.* **2011**, *13*, 045021.

[53] J. L. Webb, L. Troise, N. W. Hansen, L. F. Frellsen, C. Osterkamp, F. Jelezko, S. Jankuhn, J. Meijer, K. Berg-Sørensen, J.-F. Perrier, A. Huck, U. L. Andersen, *Phys. Rev. Appl.* **2022**, *17*, 064051.

[54] J.-C. Jaskula, K. Saha, A. Ajoy, D. Twitchen, M. Markham, P. Cappellaro, *Phys. Rev. Appl.* **2019**, *11*, 054010.

[55] C. Bonato, D. W. Berry, *Phys. Rev. A* **2017**, *95*, 052348.

[56] J. Rovny, Z. Yuan, M. Fitzpatrick, A. I. Abdalla, L. Futamura, C. Fox, M. C. Cambria, S. Kolkowitz, N. P. de Leon, *Science* **2022**, *378*, 1301.